



Supplement of

Biases in atmospheric CO₂ estimates from correlated meteorology modeling errors

S. M. Miller et al.

Correspondence to: S. M. Miller (scot.m.miller@gmail.com)

S1 The meteorological model-data assimilation framework

This section of the supplement describes the Local Ensemble Kalman Filter (LETKF) in greater detail. Many of the equations listed below are abbreviated versions of those detailed in Hunt et al. (2004), Desroziers et al. (2005), Hunt et al. (2007), Li et al. (2009), and Miyoshi (2011). For a mathematical derivation of either the meteorology optimization or covariance matrix estimation within LETKF, refer to any of those studies.

The model–data assimilation system (abbreviated CAM–LETKF) can be summarized in a number of steps. First, we create an initial condition for modeled meteorology, in this case using NCEP–DOE AMIP-II reanalysis (Kanamitsu et al., 2002). We generate a set of small perturbations to the initial conditions and use these perturbations to create a set of k initial conditions that are all slightly different. In this case, we set $k = 64$ (as in Liu et al., 2011, 2012). This choice represents a compromise between thorough statistical sampling and computational considerations: a very large k will exhaustively sample the model uncertainties. However, k CAM–CLM realizations require $4k$ computer cores, so a very large k would also become computationally prohibitive.

Second, we run a 6-hour weather forecast using CAM–CLM for each of the k model initial conditions. The spread of this model ensemble represents our prior uncertainty in the modeled meteorology:

$$\mathbf{x}_i = \bar{\mathbf{x}} + \mathbf{X}_i \quad \text{where } i = 1 \dots k \quad (\text{S1})$$

where \mathbf{x}_i ($m \times 1$) is a single model realization, $\bar{\mathbf{x}}$ ($m \times 1$) is the mean of the model ensemble, and \mathbf{X}_i ($m \times k$) refers to the i^{th} column of the matrix that defines the model ensemble spread. In the main article (e.g., Eq. 1), we defined these variables to refer to all model time steps, collectively. In the supplement, by contrast, we will instead define these variables to refer to the model–data assimilation at a single, 6 hourly time step. In other words, m and n now refer to the model outputs and number of weather observations, respectively, associated with a single model–data assimilation cycle. This redefinition of the variables facilitates a discussion of time-stepping in the remainder of this section.

Third, we calculate a set of k weights such that the weighted average of the realizations best matches the meteorological observations:

$$\bar{\mathbf{x}}^a = \bar{\mathbf{x}}^b + \mathbf{X}^b \hat{\mathbf{w}} \quad (\text{S2})$$

The superscript b refers to the model state before assimilation and a the model state after data assimilation. The $k \times 1$ vector of weights ($\hat{\mathbf{w}}$) are estimated by minimizing a statistical cost function with respect to the meteorological observations (Hunt et al., 2007):

$$J(\mathbf{w}) = (k - 1)\mathbf{w}^T \mathbf{w} + \left(\mathbf{z} - H(\bar{\mathbf{x}}^b + \mathbf{X}^b \mathbf{w}) \right)^T \mathbf{R}^{-1} \left(\mathbf{z} - H(\bar{\mathbf{x}}^b + \mathbf{X}^b \mathbf{w}) \right) \quad (\text{S3})$$

In the above equation, \mathbf{z} ($n \times 1$) represents the meteorological observations, and $H()$ is a function or operator that maps the model output to the observations. For example, the function $H()$ may convert the model units to the measurement units or may interpolate the model output to an observation site that lies between multiple model grid boxes. Lastly, the diagonal matrix \mathbf{R} ($n \times n$) represents the nugget variance, variance in the model–data residuals that is due to measurement errors or meteorological processes too small in scale to be captured by CAM–CLM.

The following equation further elucidates the role of the \mathbf{R} covariance matrix in the analysis (e.g., Hunt et al., 2007):

$$\mathbf{z} = H(\mathbf{x}) + \mathcal{N}(\mathbf{0}, \mathbf{R}) \quad (\text{S4})$$

In the above equation, \mathbf{x} refers to the true value of the meteorological parameters averaged to the resolution of the model grid. This vector is an unknown quantity, and the estimated values ($\bar{\mathbf{x}}^a$) are only a best guess of this unknown quantity. Any differences between the true, unknown values and the measurements must be due to one of two causes: either measurement error or errors due to the finite model resolution. These errors should follow a normal distribution with a mean of zero and a covariance matrix \mathbf{R} . We estimate the elements of this matrix using actual model-data residuals, as described in greater detail below.

In order to estimate the weights (\mathbf{w}), we use a localization procedure. In practice, we never compute the weights simultaneously for the entire global model output. Rather, we estimate a different set of weights for each model grid box using model-measurement pairs within a certain radius (in this case, within 1500km). As such, the matrices in Eqs. S2 and S3 represent a subset of the global model output, and the dimensions n and m are small relative to the total number of global observations and model grid boxes, respectively.

As part of this localization procedure, we interpolate the gridded model output to the observation locations and times; we use these model-measurement pairs to compute each set of weights. We further taper the influence of model-observation pairs on the optimization depending on their distance from the grid box in question (using a Blackman window function as described by Oppenheim and Schafer (1989) and Liu et al. (2012)). Hence, model-measurement pairs located within the model grid box of interest will influence the optimization much more strongly than model-observation pairs located 1000km away. A radius of 1500km for the Blackman window function is comparable to values used throughout the meteorological literature. For example, Liu et al. (2011) and Liu et al. (2012) also used a 1500km radius. Furthermore, Miyoshi (2011) set a 1825 km radius of influence, Miyoshi and Kunii (2012) used a 1460km radius, and Szunyogh et al. (2008) used an 800km radius.

This localization approach ensures coherence among adjacent grid boxes and ensures that the optimization is not an over-fit to the data. For example, if we estimated the weights using only model-measurement pairs in the grid box of interest, several problems could arise. First, there may not be many relevant observations that are sensitive to that specific grid box, particularly over the open ocean or near the poles. In those circumstances, the estimated weights could be inaccurate. Second, that approach could produce vastly different weights in adjacent grid boxes, a result that is unlikely to be physically realistic. For example, the estimated weights for one model grid box over eastern North Dakota should look somewhat similar to the weights for a grid box over western North Dakota. If the two sets of weights were completely unrelated, one could argue that the optimization would be an over-fit. A localization radius of 1500km precludes these potential problems.

The weights ($\hat{\mathbf{w}}$), estimated using this localization procedure, will have the following covariance matrix ($k \times k$) (Hunt et al., 2007):

$$\tilde{\mathbf{P}}^a = (k-1)\mathbf{I} + (\mathbf{Y}^b)^T \mathbf{R}^{-1} \mathbf{Y}^b \quad (\text{S5})$$

$$\text{where } H(\bar{\mathbf{x}}^b + \mathbf{X}^b \mathbf{w}) \approx \bar{\mathbf{y}}^b + \mathbf{Y}^b \mathbf{w} \quad (\text{S6})$$

Fourth, we generate 64 realizations that collectively represent our posterior uncertainty in the meteorology. Like the best estimate ($\bar{\mathbf{x}}^a$), these posterior realizations are also a linear combination of the prior model realizations (Hunt et al., 2007):

$$\mathbf{x}_i^a = \bar{\mathbf{x}}^a + \mathbf{X}^b \left(\left[(k-1) \tilde{\mathbf{P}}^a \right]^{\frac{1}{2}} \right)_i \quad (\text{S7})$$

where ' $\frac{1}{2}$ ' denotes the symmetric square root of the covariance matrix. The subscript i on the right hand side of the equation refers to individual columns of the matrix.

Fifth, and finally, we adjust the overall model ensemble spread to match the model uncertainties implied by the meteorological observations. We refer to this process as adaptive covariance inflation (e.g., Li et al., 2009; Miyoshi, 2011). Note that this step is new since previous CAM-LETKF studies by Liu et al. (2011) and Liu et al. (2012).

Adaptive inflation operates on the following principle: the ensemble variance and nugget variance should match against the actual model-data residuals (e.g., Li et al., 2009):

$$E \left[\left(\mathbf{z} - H(\bar{\mathbf{x}}^b) \right) \left(\mathbf{z} - H(\bar{\mathbf{x}}^b) \right)^T \right] = \mathbf{H} \mathbf{P} \mathbf{H}^T + \mathbf{R} \quad (\text{S8})$$

$$\text{where } \mathbf{P} = (k-1)^{-1} \mathbf{X}^b (\mathbf{X}^b)^T \quad (\text{S9})$$

In that equation, E denotes the expected value, and the matrix \mathbf{H} ($n \times m$) is a linearization of the function $H()$. In practice, however, these covariance matrices can diverge from the actual residuals (Refer to Miyoshi (2011) for more detail.). Therefore, we estimate a scaling factor (α) for the diagonal elements of the covariance matrix \mathbf{P} ($m \times m$). This scaling factor can be estimated by manipulating Eq. S8 as in Li et al. (2009) and Miyoshi (2011):

$$\alpha = \frac{\text{tr} \left[(\mathbf{z} - H(\bar{\mathbf{x}}^b)) (\mathbf{z} - H(\bar{\mathbf{x}}^b))^T \circ \mathbf{R}^{-1} \right] - n}{\text{tr} [\mathbf{H} \mathbf{P} \mathbf{H}^T \circ \mathbf{R}^{-1}]} \quad (\text{S10})$$

In this equation, tr refers to the matrix trace, and the symbol \circ indicates element-wise multiplication. The result of Eq. S10 is then weighted against the scaling factor from the previous model time step to produce a final scaling factor estimate (refer to Li et al., 2009; Miyoshi, 2011).

To date, the use of a single scaling factor (α) per grid box has been a standard practice in ensemble Kalman filters applied to weather models (e.g., Szunyogh et al., 2008; Liu et al., 2011, 2012; Miyoshi and Kunii, 2012; Kang et al., 2012), and we do the same here. When we estimate a single scaling factor per box, we leverage more observations to make a more stable inflation estimate. Otherwise, adaptive inflation can become challenging to implement; adaptive inflation performs poorly when observations are sparse (e.g., Miyoshi, 2011).

We also estimate the nugget variance ($\sigma_{\mathbf{R},j}^2$) for a given observation type (j) using the model output and observations (Desroziers et al., 2005; Li et al., 2009):

$$\sigma_{\mathbf{R},j}^2 = \frac{(\mathbf{z}_j - H(\bar{\mathbf{x}}^a))^T (\mathbf{z}_j - H(\bar{\mathbf{x}}^b))}{n_j} \quad (\text{S11})$$

As with α , the result in Eq. S11 is also weighted against the estimated variance from the previous time step to produce a final variance estimate (Li et al., 2009). Unlike the localized LETKF calculations, we estimate a single nugget variance for the entire globe (for each meteorological observation type). In other words, in Eq. S11, the inputs represent global values for observation type j , not a localized implementation as in previous equations.

After these steps, the model-assimilation cycle begins again with another 6-hour CAM-CLM forecast. The posterior ensemble members (\mathbf{x}_i^a) become the initial conditions for this next CAM-CLM forecast.

In our study, we utilize biospheric, oceanic, biomass burning, and fossil fuel CO₂ fluxes from CarbonTracker (CT), and we do not change these fluxes in response to any parameters within CAM-CLM. The original CT fluxes have a temporal resolution of 3 h. We average these fluxes to a 6 h resolution for all of the CAM-CLM simulations in this study, the length of each model time step.

Furthermore, we use CT as the initial condition for global atmospheric CO₂ mixing ratios on 1 January and 1 May 2009. Each CAM ensemble member uses the same initial condition for atmospheric CO₂, so any subsequent differences in CO₂ among the model realizations are due entirely to meteorological uncertainties.

S2 CAM–LETKF performance metrics

The paragraphs that follow discuss two different metrics of CAM–LETKF performance: large-scale meteorology model–data comparisons and a more in-depth view of the estimated variances (i.e., the variance inflation and the nugget variance).

First, we examine the meteorology model–data residuals for the model best-guess (\bar{x}^a). Figure S1 displays the root mean squared model–measurement error (RMSE, $\sqrt{(1/n) \sum (\mathbf{y} - H(\bar{x}^a))^2}$), broken down by time and by observation type. Each point plotted in Fig. S1 is the RMSE computed from all available global observations. This RMSE appears comparable in magnitude to several existing weather reanalysis products. For example, these statistics are similar to CAM-LETKF simulations by Liu et al. (2011), though simulations in that paper cover a much shorter time period. Furthermore, the temperature, pressure, and wind errors reported here are in the range of those listed for North American Regional Reanalysis (NARR) and ERA-Interim reanalysis (Mesinger et al., 2006; Dee et al., 2011).

The remainder of this section discusses the estimated covariance matrix parameters. Fig. S2 displays a map of the average variance inflation factors (α) in the model surface layer for February and July, 2009, and Fig. S3 shows how the average variance inflation factor changes over time through five months of CAM–LETKF simulations.

These figures show several notable patterns, three of which we discuss in more detail. First, the inflation factors in Fig. S2 are highest over North America, Asia, and Australia, regions with relatively abundant meteorological observations. A number of previous studies confirm this positive relationship between data density and covariance inflation (e.g., Anderson, 2009; Miyoshi, 2011; Miyoshi and Kunii, 2012). Furthermore, Miyoshi (2011) points out that a high inflation factor in observation-rich regions may cause the ensemble spread to be too large downwind. This explanation may account for the adjacent regions of high inflation (over continents) and low inflation (over the oceans) in Fig. S2.

Second, the global average of the inflation factors is less than one (Fig. S3). Even though the inflation factors, on average, decrease the ensemble variance, the global ensemble variance remains relatively constant over time. For example, the average 6 hourly model ensemble spread at meteorology observation sites is comparable in February, June, and July: $\sim 1.5 \text{ m s}^{-1}$ for zonal and meridional wind (standard deviation), $\sim 0.7 \text{ K}$ for surface temperature, and $\sim 1.1 \text{ mb}$ for surface pressure. This consistency, in spite of the small inflation average, may be due to the nonlinear nature of the meteorological model – differences among individual ensemble members can escalate or intensify over the 6-hour meteorology forecast.

A third notable feature is the low inflation values over eastern, tropical Pacific Ocean. These low values are intentional by design; we set a very low initial estimate for the variance inflation in this region of the globe. Higher inflation values cause the ensemble variance to increase rapidly in this region and lead to unphysical temperature estimates near the tropopause. This issue is due to an enigmatic temperature instability in the meteorological model. In the forecast stage of the CAM model, the ensemble’s temperature spread in this region can increase rapidly if the initial conditions (i.e., the posterior ensemble from the previous time step) have a sufficiently large spread.

Normally, one might expect the adaptive inflation to correct for this issue; the adaptive inflation adjusts the variance of the meteorology model ensemble to match the actual model-

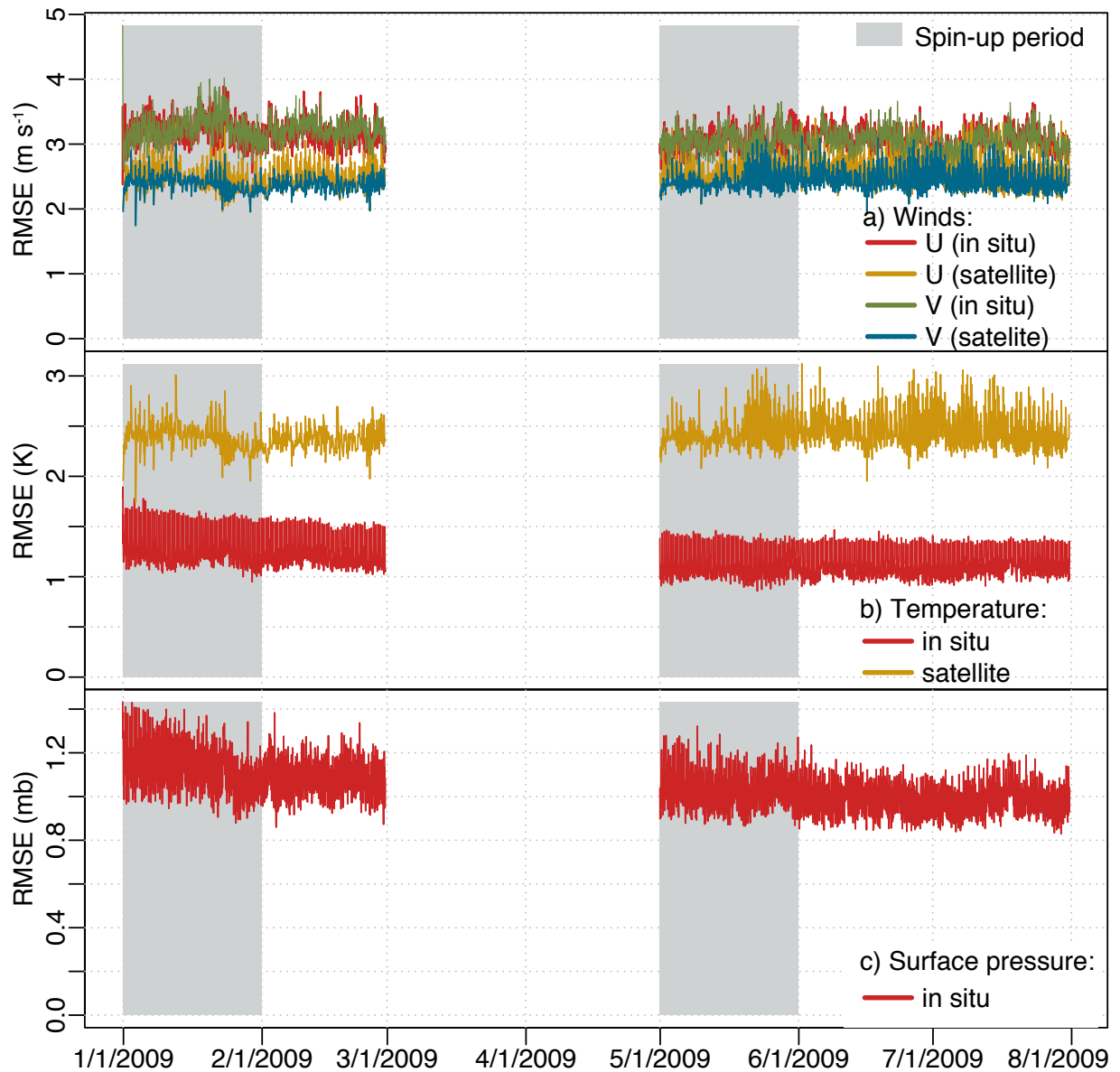


Figure S1: Root mean squared errors for the CAM-LETKF best estimate compared against various meteorological observations (RMSE, $\sqrt{(1/n) \sum (\mathbf{y} - H(\bar{\mathbf{x}}^a))^2}$).

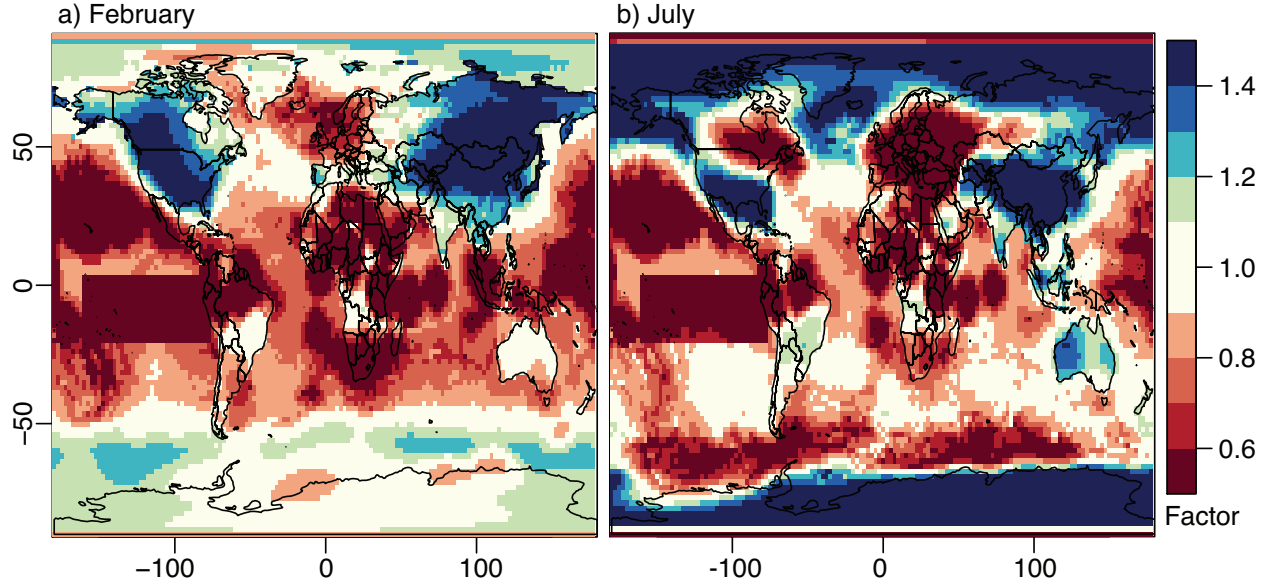


Figure S2: The variance inflation factors for the CAM model surface layer, averaged over each 6 hourly estimation period in February and July, 2009. In this study, we estimate a different inflation factor for each model grid box and each 6 hourly estimation period. More specifically, we estimate a single inflation factor for all model parameters (e.g., wind, temperature, surface pressure, and specific humidity) in each box.

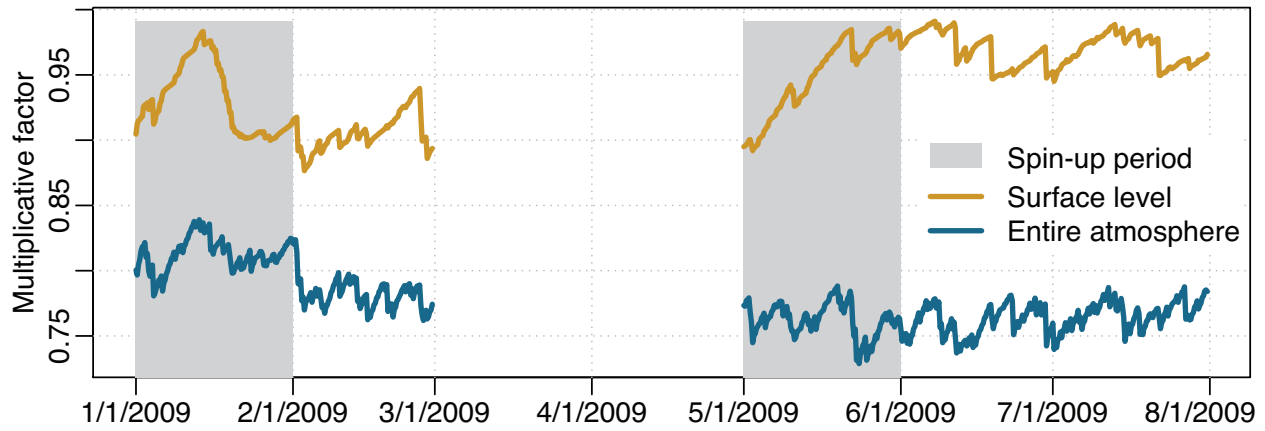


Figure S3: Time series of the average variance inflation factors, both at the surface and for all vertical model levels. The inflation factors show some variability during the model spin-up periods, then stabilize to relatively constant values.

data residuals. In theory, this procedure should prevent the ensemble spread from exploding (given sufficient data). However, the inflation factor, by design, cannot change suddenly from one time step to another. The adaptive inflation procedure uses the previous time step as the prior inflation estimate, and that prior estimate has a finite uncertainty (in this case, a prior standard deviation of 0.03 – similar to the values used by Miyoshi (2011)). Because of this prior uncertainty, the adaptive inflation factor must evolve slowly over many days if it changes at all. In most cases, this property is desirable because it prevents a small number of observations from making dramatic changes to the evolution of the model-data system. However, in the case of this temperature instability, the instability in the model develops over 4-5 model time steps, much faster than the response time of the adaptive inflation factor.

The adaptive inflation procedure requires an initial inflation estimate for the first time step of the model run (i.e., an initial condition). The adaptive procedure then updates this estimate at each model time step (e.g., Eq. S10). For this initial estimate or initial condition, we set a small value (0.4) for the equatorial western Pacific. During the one-month model spin-up period, the estimated inflation value evolves substantially from the initial estimate in most regions of the globe (e.g., Fig. S3). Over this region of the Pacific, however, the estimated inflation factor does not evolve or change very much; either this initial estimate is consistent with the actual model-data residuals, or the meteorological data (and the adaptive inflation procedure) are not very informative over the region. In either case, this small initial condition prevents the ensemble spread from becoming unstable over the region.

In addition to the covariance inflation, the nugget variance also remains consistent over time. Fig. S4 shows the square root of the nugget variance for each observation type and at each model time period. Note that we estimate different values of the nugget variances by observation type and time, but the estimated variances are spatially constant across the globe. These estimates remain consistent over time, except for the initial January spin-up period, during which the estimate slowly evolves from the initial guess.

S3 Uncertainties in atmospheric CO₂ transport

This section of the supplement provides more detailed plots of the CO₂ transport uncertainties shown in Fig. 2 of the main article. In particular, the plots in this section (Figs. S5 – S8) visualize the transport uncertainties for different time slices of the day and show how CO₂ transport uncertainties differ between day and nighttime. The first two figures (Figs. S5 and S6) display the mean 6 hourly CO₂ transport uncertainties for February and July, 2009, a setup analogous to Figs. 2a-b in the main manuscript. Conversely, Figs. S7 and S8 exhibit the uncertainties in the month-long mean CO₂ concentrations, analogous to Figs. 2c-d in the main article.

In general, the 6 hourly uncertainties vary widely depending on the local time with higher uncertainties at night (Figs. S5 and S6). Note that case study one in the main article (sections 2.4 and 3.3) only uses model output associated with local afternoon CO₂ measurements. In contrast to these 6 hourly uncertainties, the uncertainties in monthly-mean concentrations do not vary as much by time of day (Figs. S7 and S8). For example, over North America and northern Eurasia in February, the CO₂ uncertainties are equally high during all times of day. However, a diurnal cycle in the month-long uncertainties is apparent over some regions – equatorial Africa, South America, and over Northern Hemisphere land regions in summer.

These transport uncertainties are in the range of the uncertainties estimated in a number of previous studies. For example, the spatial patterns in the 6 hourly uncertainties are similar to those modeled by Liu et al. (2011) using CAM-LETKF and temperature-scaled CO₂ fluxes from TRANSCOM 3. In addition, a number of previous studies focused on the effects of

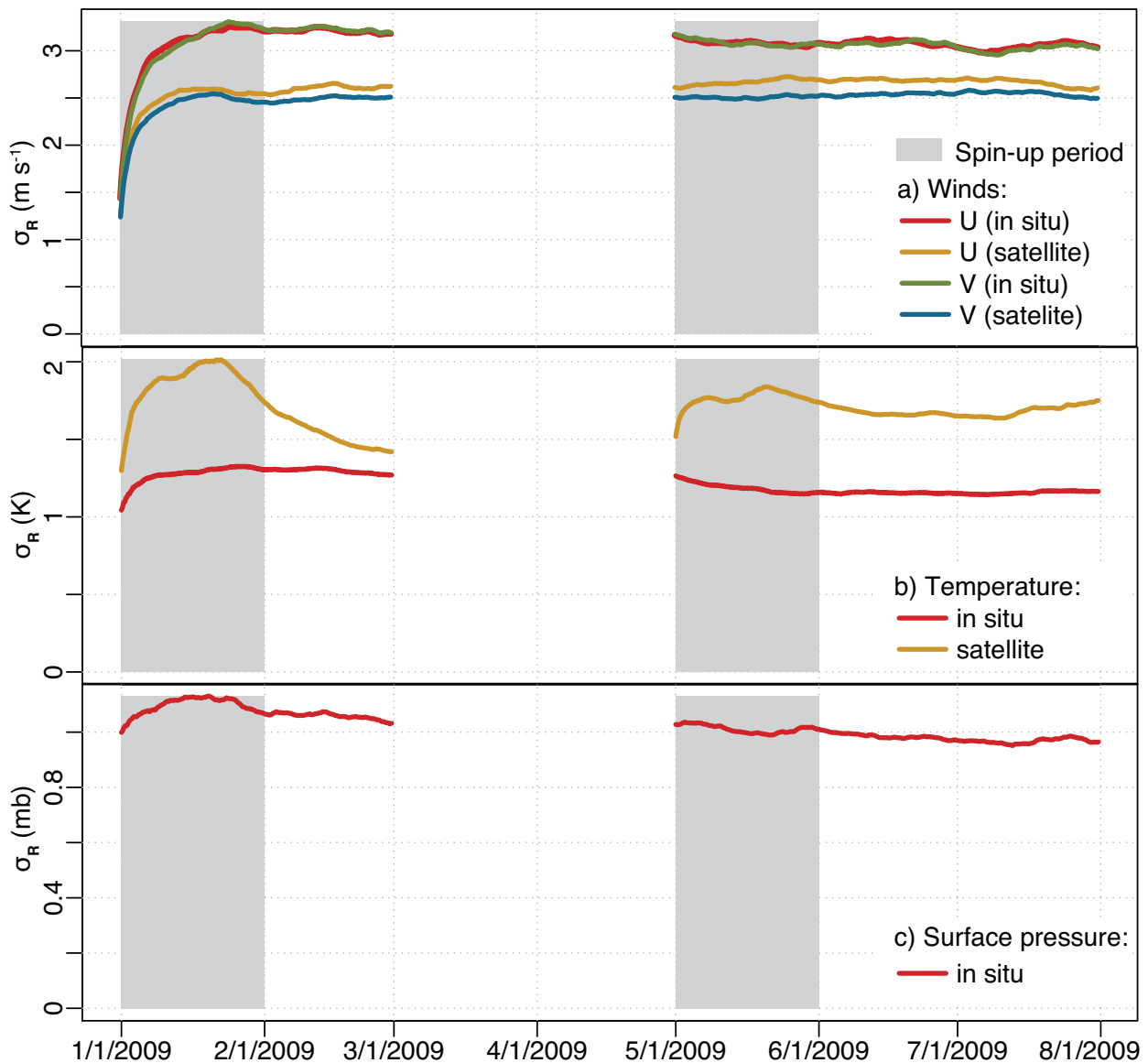


Figure S4: The square root of the nugget variance (σ_R^2) estimated within CAM-LETKF.

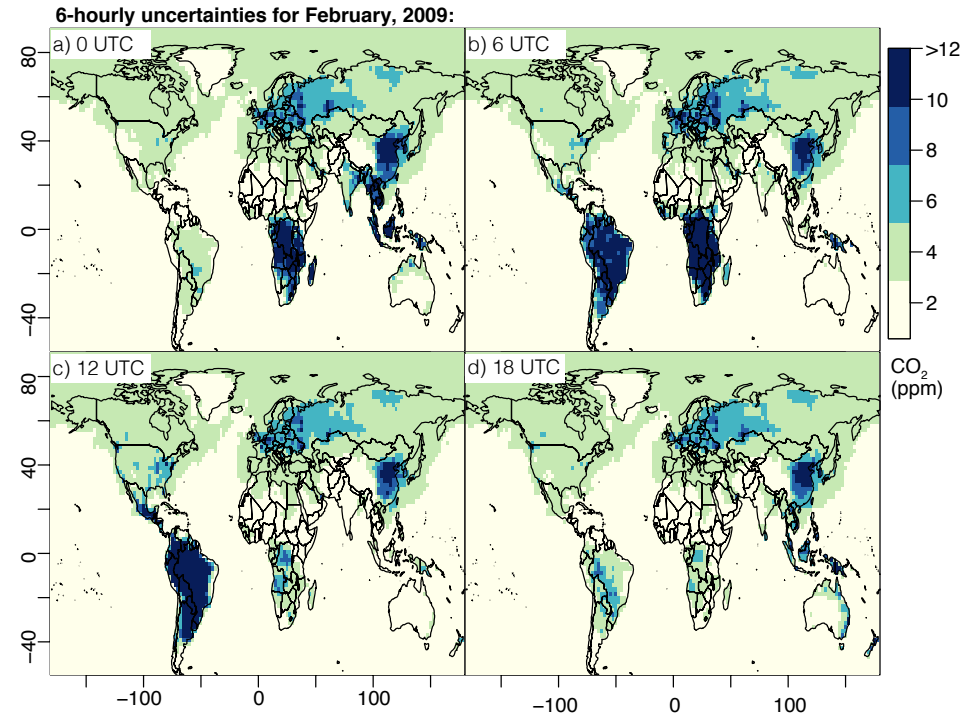


Figure S5: This figure displays the average 6 hourly CO₂ transport uncertainties in the model surface layer for a) 0 UTC, b) 6 UTC, c) 12 UTC, and d) 18 UTC. This figure is similar to Fig. 2a in the main manuscript except the uncertainties (95% confidence interval) shown here are disaggregated by time of day.

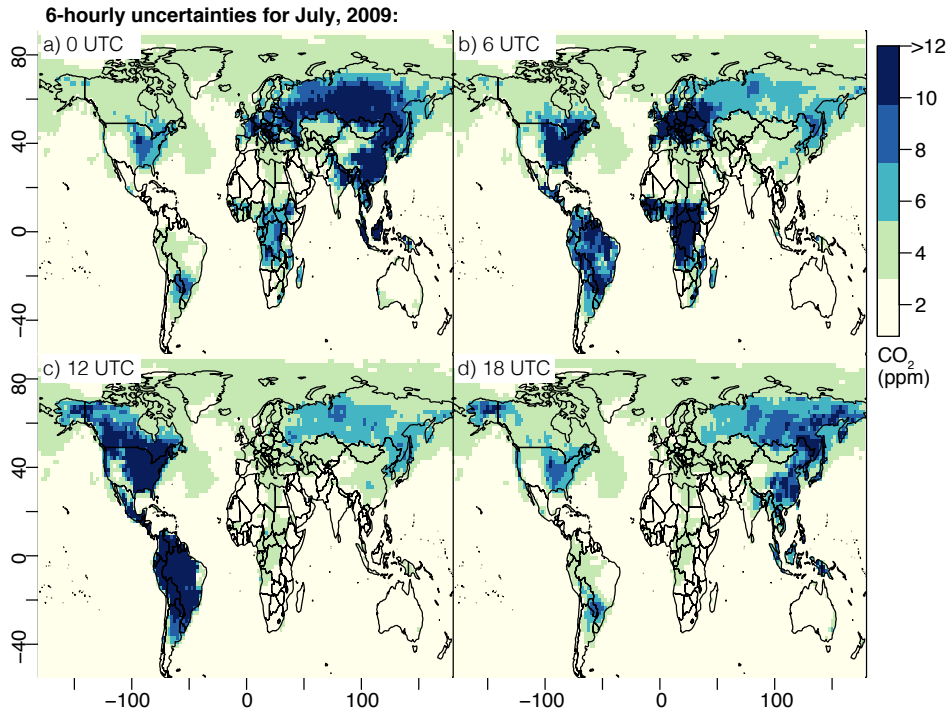


Figure S6: The CO₂ transport uncertainties for July, 2009, analogous to Fig. S5 but for a different time period.

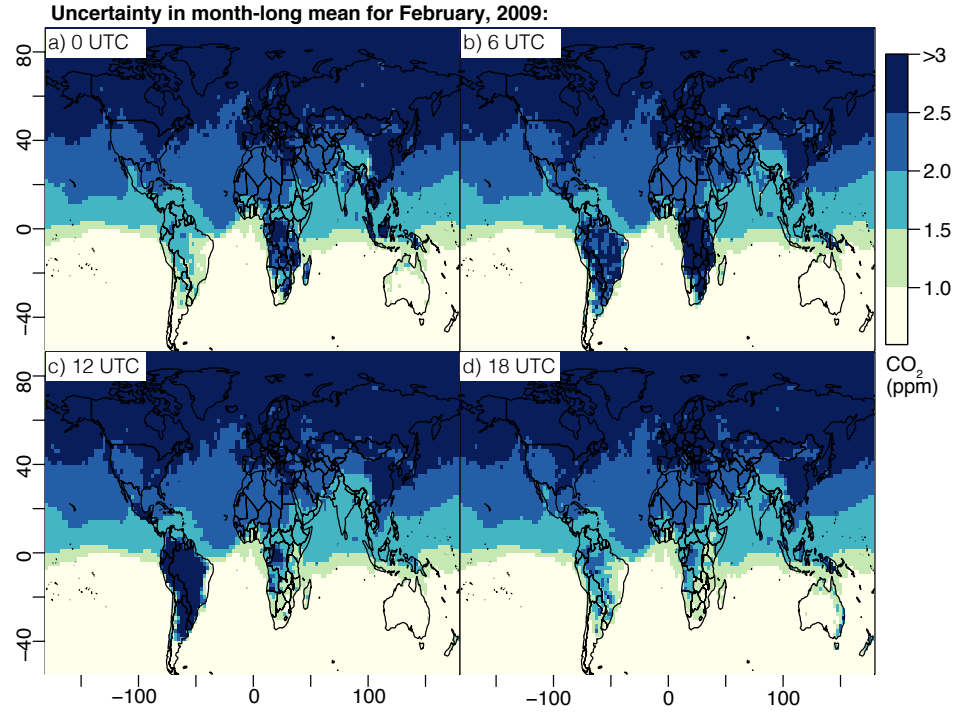


Figure S7: Uncertainties (95% confidence interval) in the monthly-averaged surface CO₂ concentrations for February, 2009. This figure is similar to Figs. 2c in the main article except the uncertainties are broken down by time of day for a) 0 UTC, b) 6 UTC, c) 12 UTC, and d) 18 UTC.

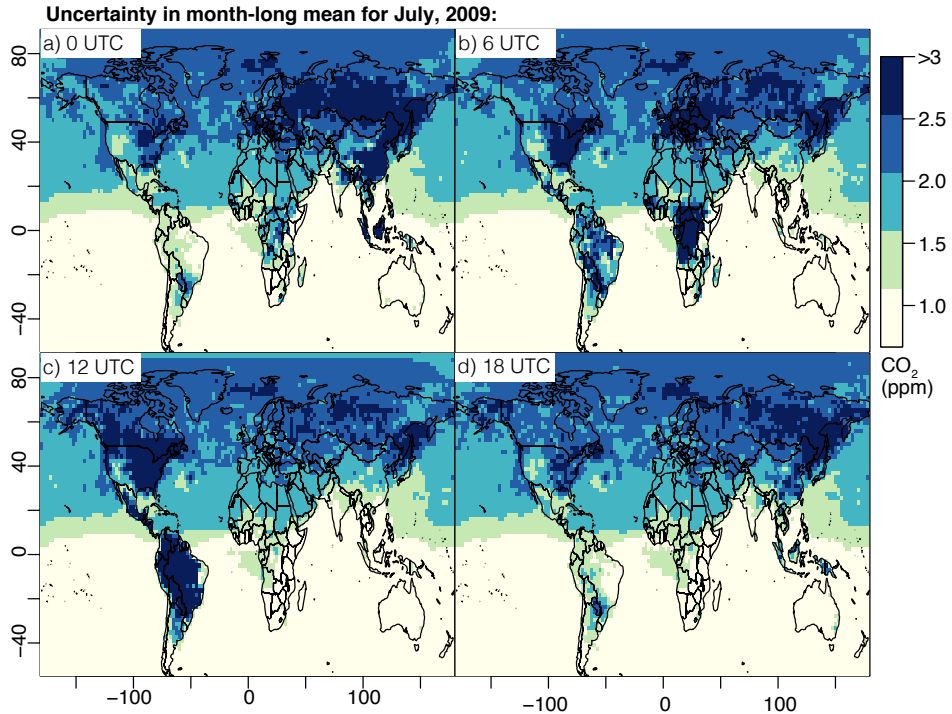


Figure S8: Uncertainties in the monthly-averaged surface CO₂ concentrations for July, 2009.

perturbing individual meteorological parameters at specific observation sites or for individual aircraft campaigns (e.g., Gerbig et al., 2003, 2008; Lin and Gerbig, 2005; Kretschmer et al., 2012). Our 6 hourly transport uncertainties, though very different in both scope and scale, are comparable in magnitude to the individual parameter uncertainties estimated by Gerbig et al. (2003), Gerbig et al. (2008), and Kretschmer et al. (2012) but are less than the uncertainties in Lin and Gerbig (2005). Furthermore, our estimated 6 hourly transport uncertainties also appear similar to or slightly smaller than the model–data mismatch errors estimated at individual observation sites in several inversion studies (e.g., Peters et al., 2007; Schuh et al., 2010; Gourdji et al., 2012). Model–data mismatch includes not only transport errors but also any model or data errors unrelated to an imperfect initial flux estimate. This result may reflect the fact that atmospheric transport often dominates model–data mismatch errors.

S4 CO₂ observation sites

This section lists the geographic locations of the measurement sites used for case study one in the main article (Figs. 4–5). Note that this case study does not use actual data from these observation sites, only model output generated for these locations. These observation site locations are available from the GAWSIS Station Information System (MeteoSwiss Federal Office of Meteorology and Climatology, 2014). The sites below are grouped by ecoregion, and the regions used here are defined by Olson et al. (2001).

Table S1: A list of observation sites used for the analysis in Figs. 4–5. All measurement sites are towers unless otherwise noted.

| Site | Code | Lat. (°N) | Lon. (°) | Alt. (m) |
|---|------|-----------|----------|----------|
| <i>East Asian temperate broadleaf and mixed forests</i> | | | | |
| Anmyeon-do, Korea | AMY | 36.5 | 126.3 | 47 |
| Gosan, Korea | GSN | 33.3 | 126.2 | 72 |
| Kisai, Japan | KIS | 36.1 | 139.6 | 13 |
| Mikawa-Ichinomiya, Japan | MKW | 34.9 | 137.4 | 50 |
| Mount Dodaira, Japan | DDR | 36.0 | 139.2 | 840 |
| Ryori, Japan | RYO | 39.0 | 141.8 | 260 |
| <i>European temperate broadleaf and mixed forests</i> | | | | |
| Bialystok, Poland | BIK | 53.1 | 23.0 | 183 |
| Cesar, Netherlands | CBW | 52.0 | 4.9 | -2 |
| Diabla Gora, Poland | DIG | 54.2 | 22.1 | 157 |
| Gif sur Yvette, France | GIF | 48.7 | 2.1 | 167 |
| Hegyhatsal, Hungary | HUN | 47.0 | 16.7 | 248 |
| Heidelberg, Germany | HEI | 49.4 | 8.7 | 116 |
| Hohenpeissenberg, Germany | HPB | 47.8 | 11.02 | 985 |
| Kollumerwaard, Netherlands | KMW | 53.3 | 6.3 | 0 |
| Mace Head, Ireland | MHD | 53.3 | -9.9 | 8 |
| Moussala, Bulgaria | BEO | 42.2 | 23.6 | 2925 |
| Neuglobsow, Germany | NGL | 53.2 | 13.0 | 65 |
| Norunda, Sweden | NOR | 60.0 | 17.3 | 70 |
| Ochsenkopf, Germany | OXK | 50.0 | 11.8 | 1185 |
| Orleans, France | TRN | 48.0 | 2.1 | 131 |

| | | | | |
|---|-----|-------|--------|------|
| Puy de Dome, France | PUY | 45.8 | 3.0 | 1465 |
| Schauinsland, Germany | SSL | 47.92 | 7.92 | 1205 |
| Tall Tower Angus, United Kingdom | TTA | 56.6 | 3.0 | 400 |
| <i>North American temperate broadleaf and mixed forests</i> | | | | |
| Argyle, Maine, US | AMT | 45.0 | 68.7 | 50 |
| Beech Island, South Carolina, US | SCT | 33.4 | 81.8 | 115 |
| Egbert, Ontario, Canada | EGB | 44.2 | -79.8 | 253 |
| Park Falls, Wisconsin, US (tower/aircraft) | LEF | 46.0 | 90.3 | 472 |
| Shenandoah National Park, Virginia | SNP | 38.6 | 78.4 | 1008 |
| Worchester, Massachusetts, US (aircraft) | NHA | 43.0 | -70.6 | 0 |
| <i>North American boreal forests / taiga</i> | | | | |
| Candle Lake, Sask., Canada | CDL | 53.9 | -104.7 | 489 |
| Chibouguau, Quebec, Canada | CHM | 49.7 | 74.3 | 393 |
| East Trout Lake, Sask., Canada (tower/aircraft) | ETL | 54.4 | -105.0 | 492 |
| Fraserdale, Ontario, Canada | FSD | 49.9 | -81.6 | 210 |
| Poker Flats, Alaska, US (aircraft) | PFA | 65.1 | -147.3 | 210 |
| <i>North American temperate grasslands, savannas and shrublands</i> | | | | |
| Beaver Crossing, Nebraska (aircraft) | BNE | 40.8 | -97.3 | 466 |
| Bondville, Illinois, US (aircraft) | AAO | 40.1 | -88.4 | 230 |
| Boulder, Colorado, US | BAO | 40.1 | -105.0 | 1584 |
| Briggsdale, Colorado (aircraft) | CAR | 40.4 | -104.3 | 1740 |
| Dahlen, North Dakota (aircraft) | DND | 47.5 | -99.2 | 472 |
| Lac La Biche, Alberta, Canada | LLB | 55.0 | -112.5 | 540 |
| Southern Great Plains, Oklahoma, US (tower/aircraft) | SGP | 36.78 | -97.5 | 314 |
| Moody, Texas, US | WKT | 31.3 | 97.3 | 251 |
| Walnut Grove, California, US | WGC | 38.3 | 121.5 | 0 |
| West Branch, Iowa, US (tower and aircraft) | WBI | 41.7 | 91.4 | 242 |

S5 CO₂ model-data comparisons

In this portion of the supplement, we show several CO₂ model and data time series from different types of observation sites (Figs. S9 – S14). These plots illustrate the capacity of CAM-LETKF (paired with CarbonTracker fluxes) to reproduce hourly-averaged CO₂ observations. Furthermore, the plots provide greater context on the CO₂ ensemble spread. The top panel of each figure illustrates the ensemble mean and ensemble spread. The bottom panel shows the modeled CO₂ boundary layer enhancement – modeled CO₂ at the observation site minus modeled concentrations at 600 hPa. This enhancement approximates the CO₂ contribution from regional surface fluxes. This increment is used for case study one in the main paper (section 2.4). In general, the modeled contribution of regional fluxes is largest during summer where biosphere uptake is strongest (e.g., LEF and AMT).

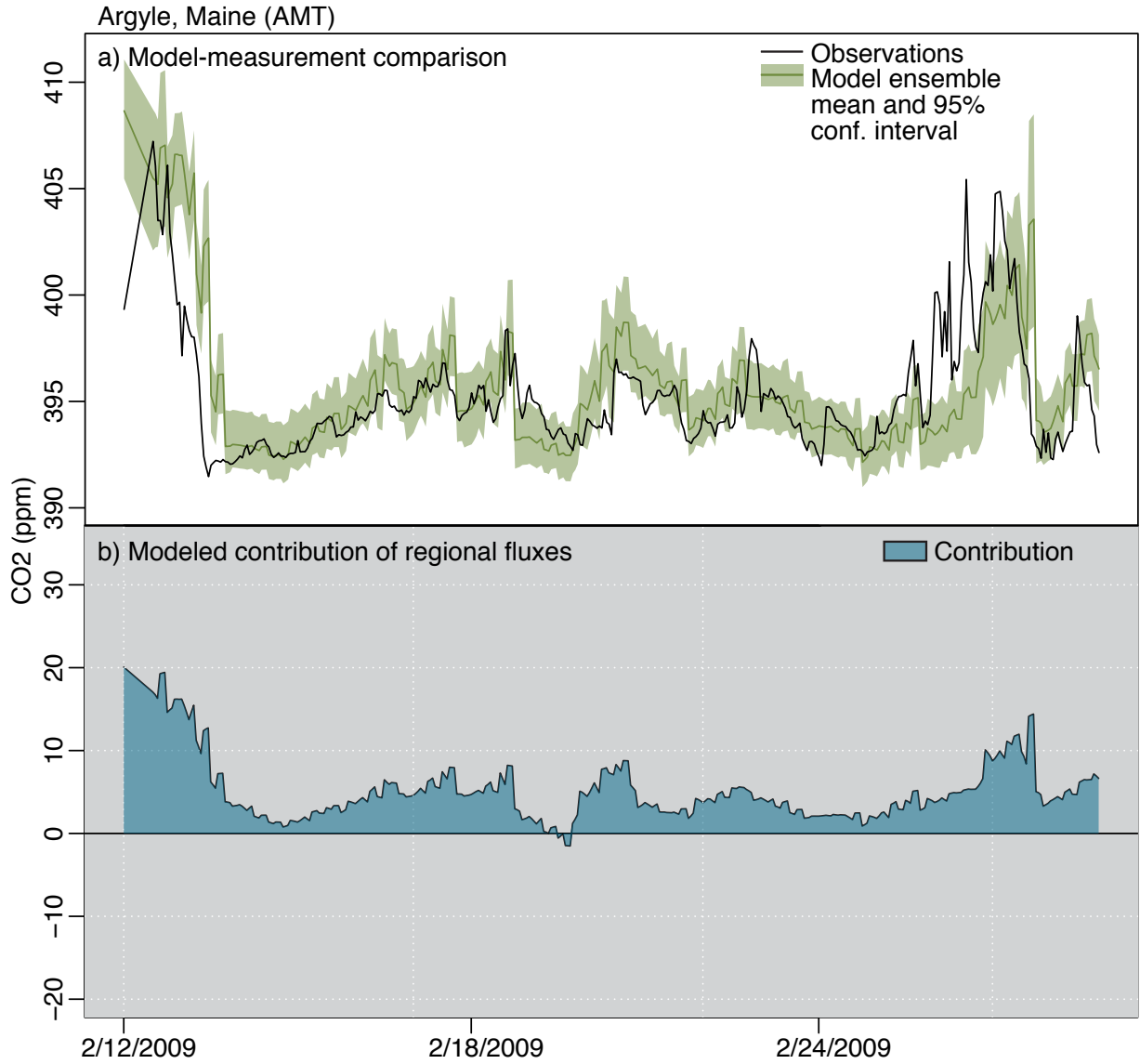


Figure S9: Panel (a) displays the hourly-averaged CO₂ measurements at Argyle tower, Maine, and the modeled CO₂ time series using CAM-LETKF and CarbonTracker fluxes. Panel (b) shows the estimated contribution of regional CO₂ fluxes at the observation site. Here, we define this contribution as modeled CO₂ at the surface minus modeled CO₂ at 600 hPa.

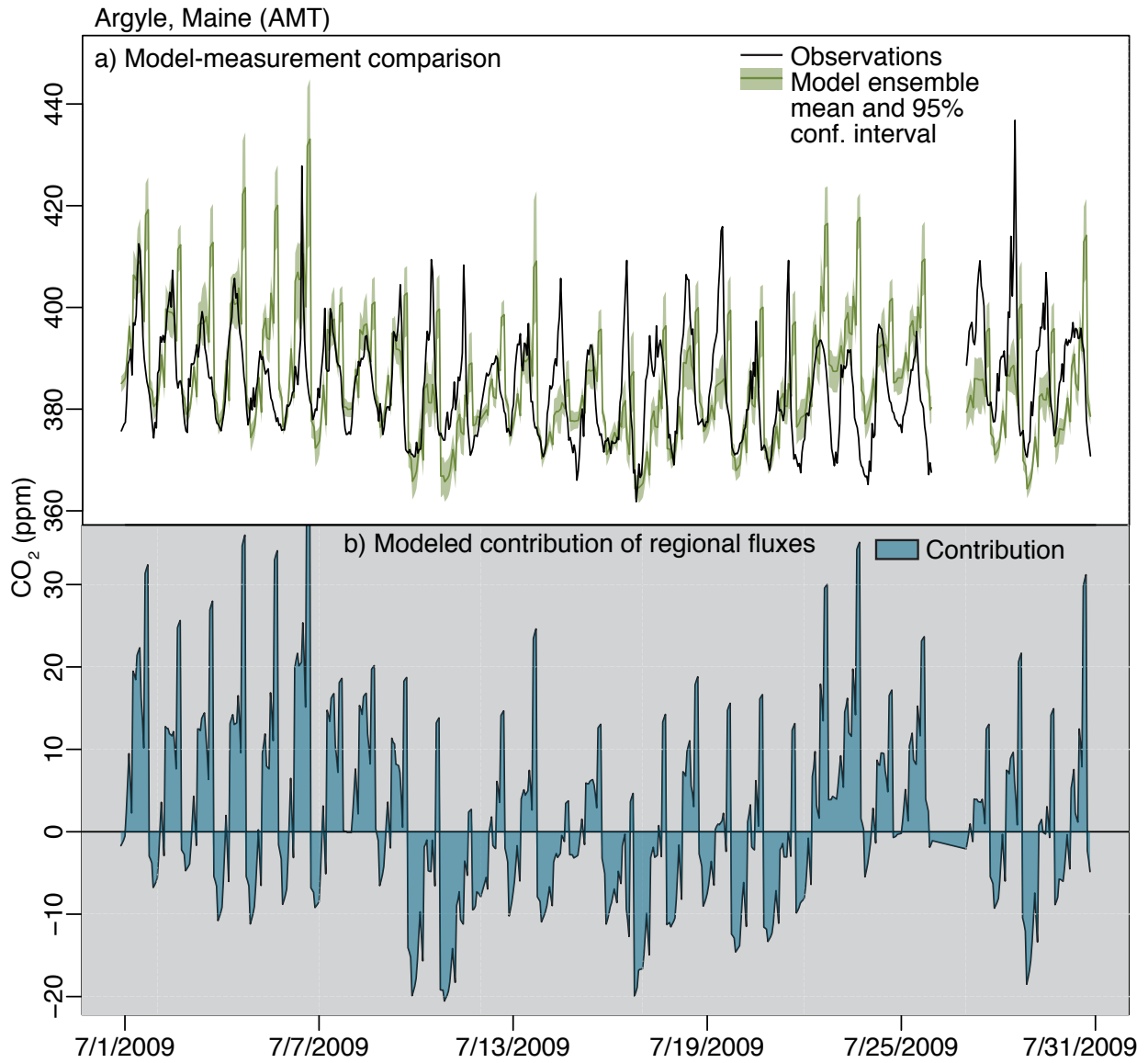


Figure S10: This figure is analogous to Fig. S9 but the Argyle tower in July 2009. Note that the top panel of each time-series plot (Figs. S9a– S14a) has a different y-axis, but the bottom panels (Figs. S9b– S14b) all have the same y–axis.

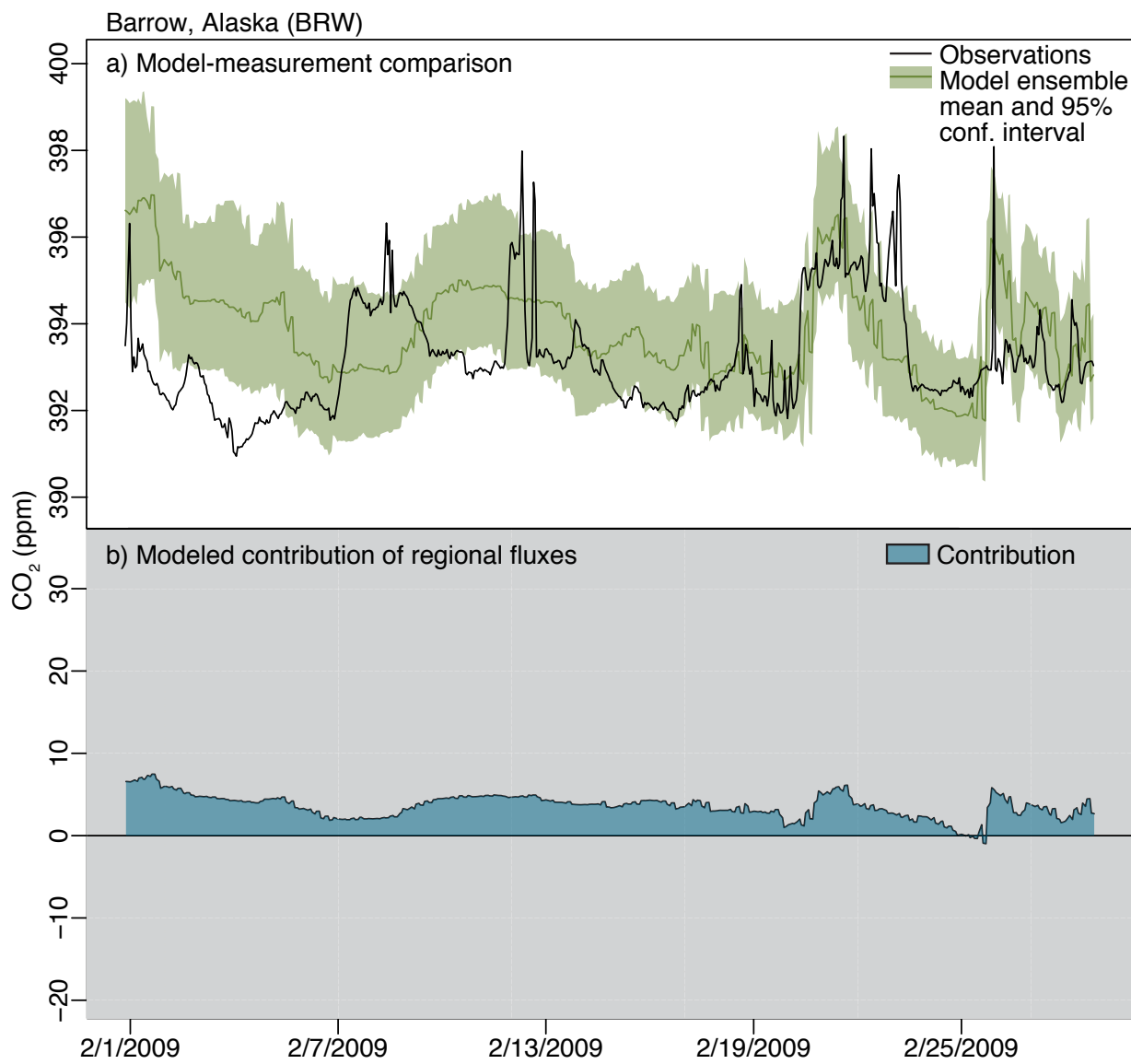


Figure S11: This figure is analogous to Fig. S9 but the Barrow, Alaska, in February 2009.

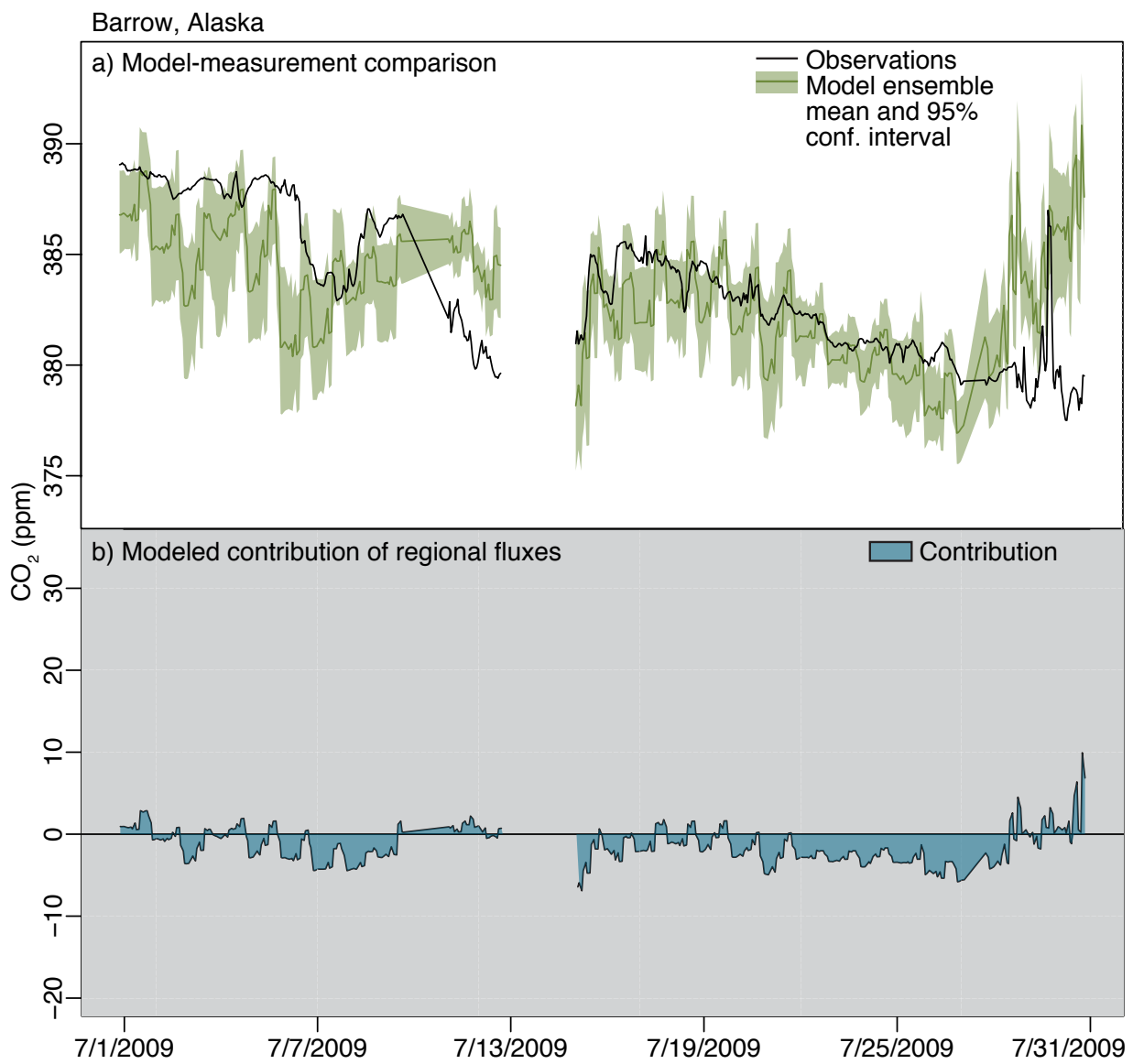


Figure S12: This figure is analogous to Fig. S9 but the Barrow, Alaska, in July 2009.

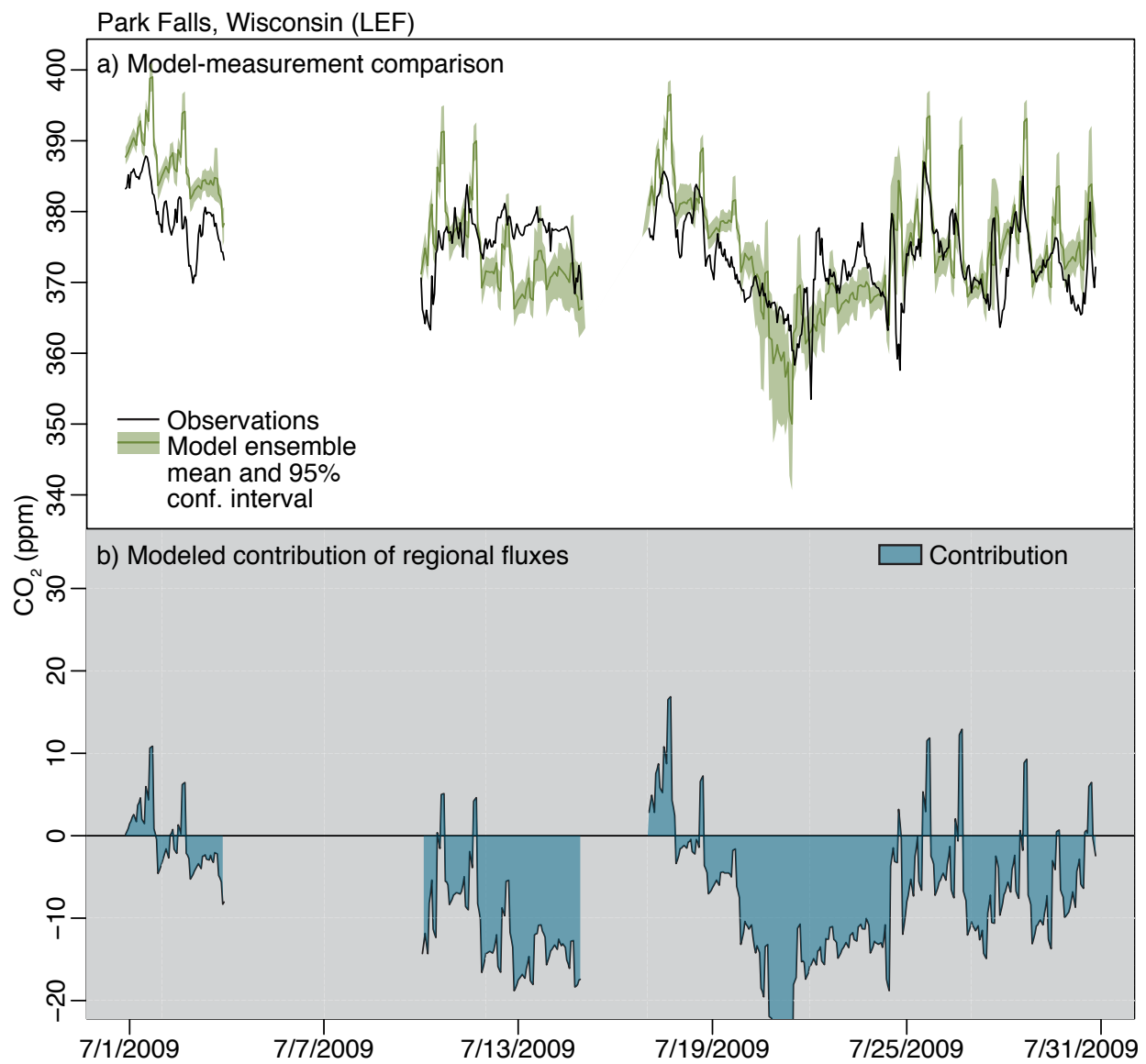


Figure S13: This figure is analogous to Fig. S9 but for Park Falls, Wisconsin, in July 2009.

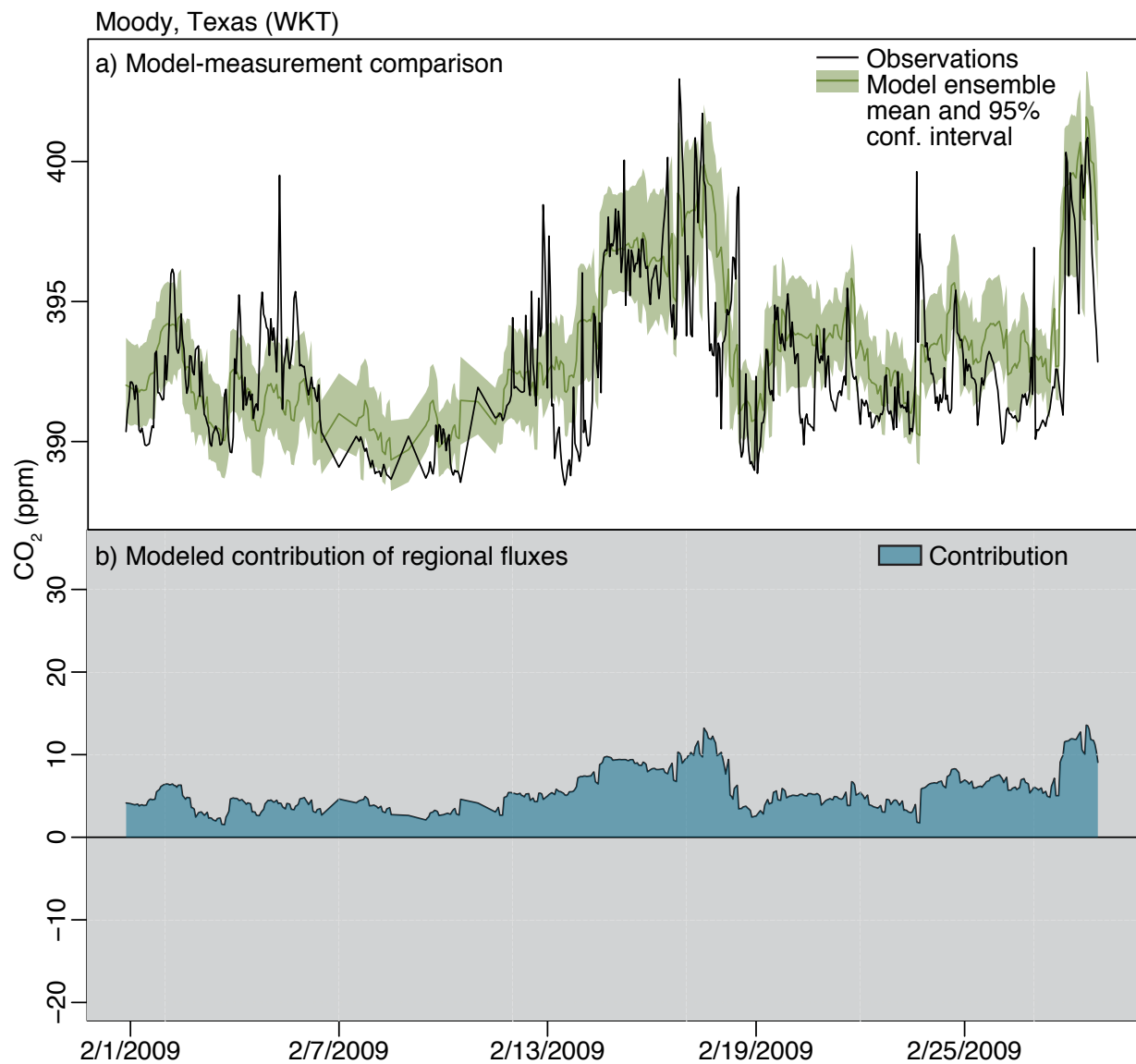


Figure S14: This figure is analogous to Fig. S9 but for Moody, Texas, in February 2009.

S6 Plots of meteorological variables and uncertainties

This section describes, in greater detail, the monthly-averaged meteorological parameters considered in the synthetic tracer experiment (case study two, sections 2.5 and 3.4). Table S2 lists all of the meteorological parameters that we compare against the synthetic tracer CV. We compare the synthetic tracer against the monthly-averaged meteorological parameters, the standard deviation in the monthly mean parameters, and the CV of each meteorological parameter – 60 parameters in total.

Figures S15-S17 display a number of monthly-averaged meteorological parameters estimated by CAM-LETKF – both those listed in section 3.4 and several additional variables for reference. For example, these figures display monthly mean zonal and meridional winds, and the uncertainties (standard deviation) (Fig. S17). These uncertainties exhibit a number of patterns consistent with well-known meso- and synoptic-scale circulation patterns. For example, the uncertainty in zonal winds is generally higher in many coastal regions including the west coast of North and South America. These patterns may reflect uncertainties in modeled sea breezes. Uncertainties in the zonal surface winds are also higher over many mountainous regions, including the US Rocky Mountains and Himalayas. These uncertainties may reflect the challenges of modeling winds over complex terrain. In addition, uncertainties in both zonal and meridional surface winds are higher along the Intertropical Convergence Zone (ITCZ).

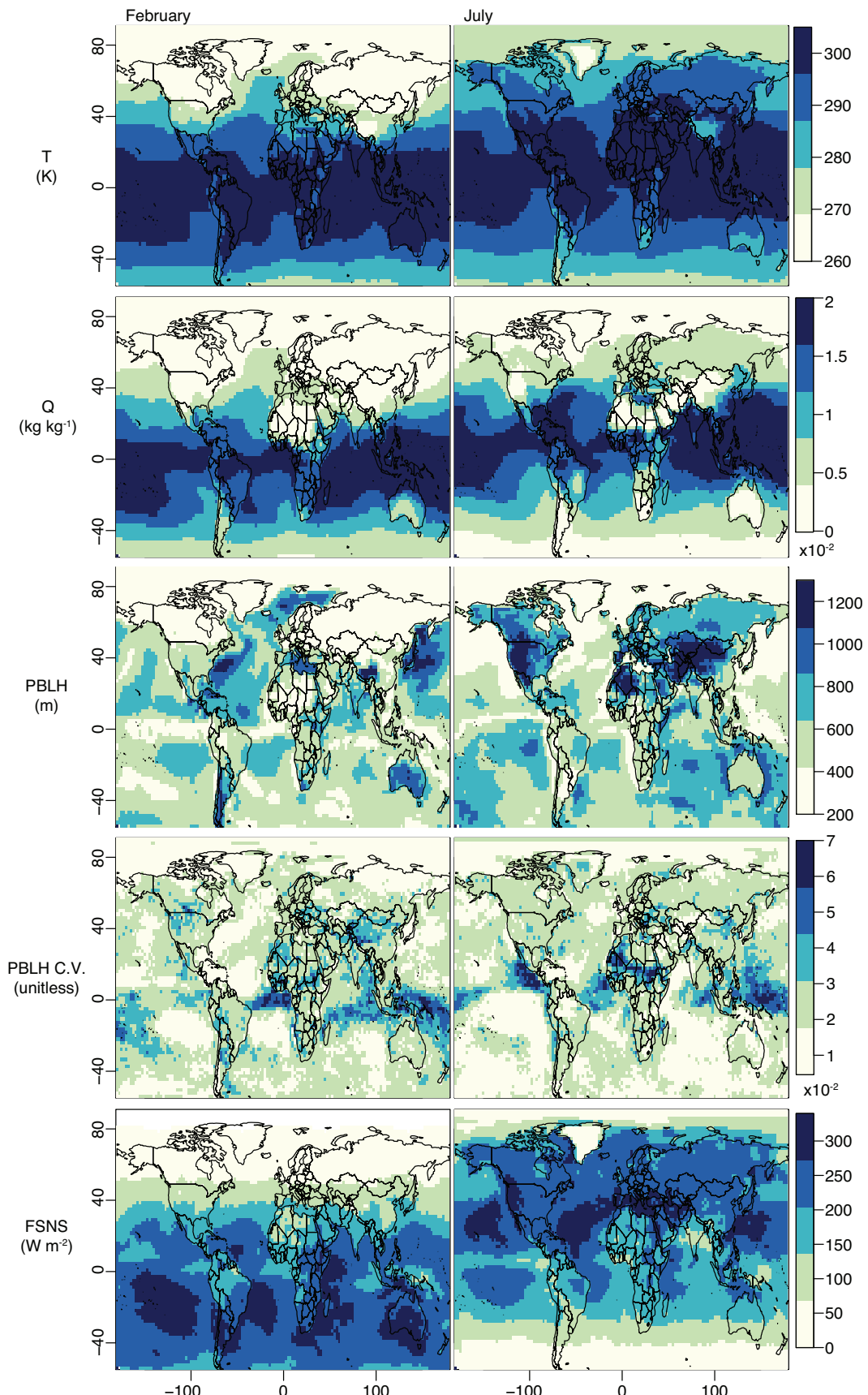


Figure S15: Maps of monthly-averaged meteorological parameters as estimated by CAM-LETKF.

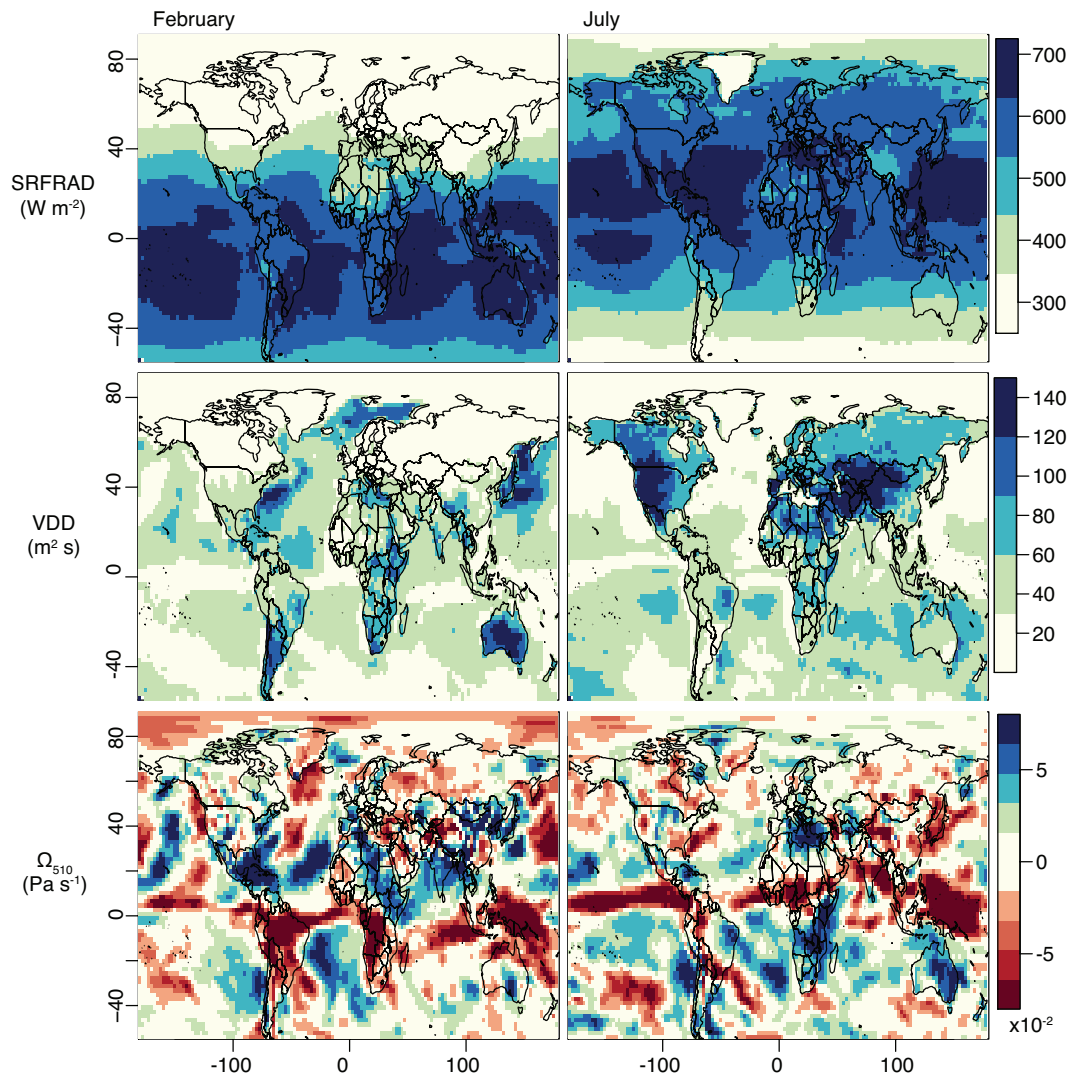


Figure S16: Maps of monthly-averaged meteorological parameters as estimated by CAM-LETKF.

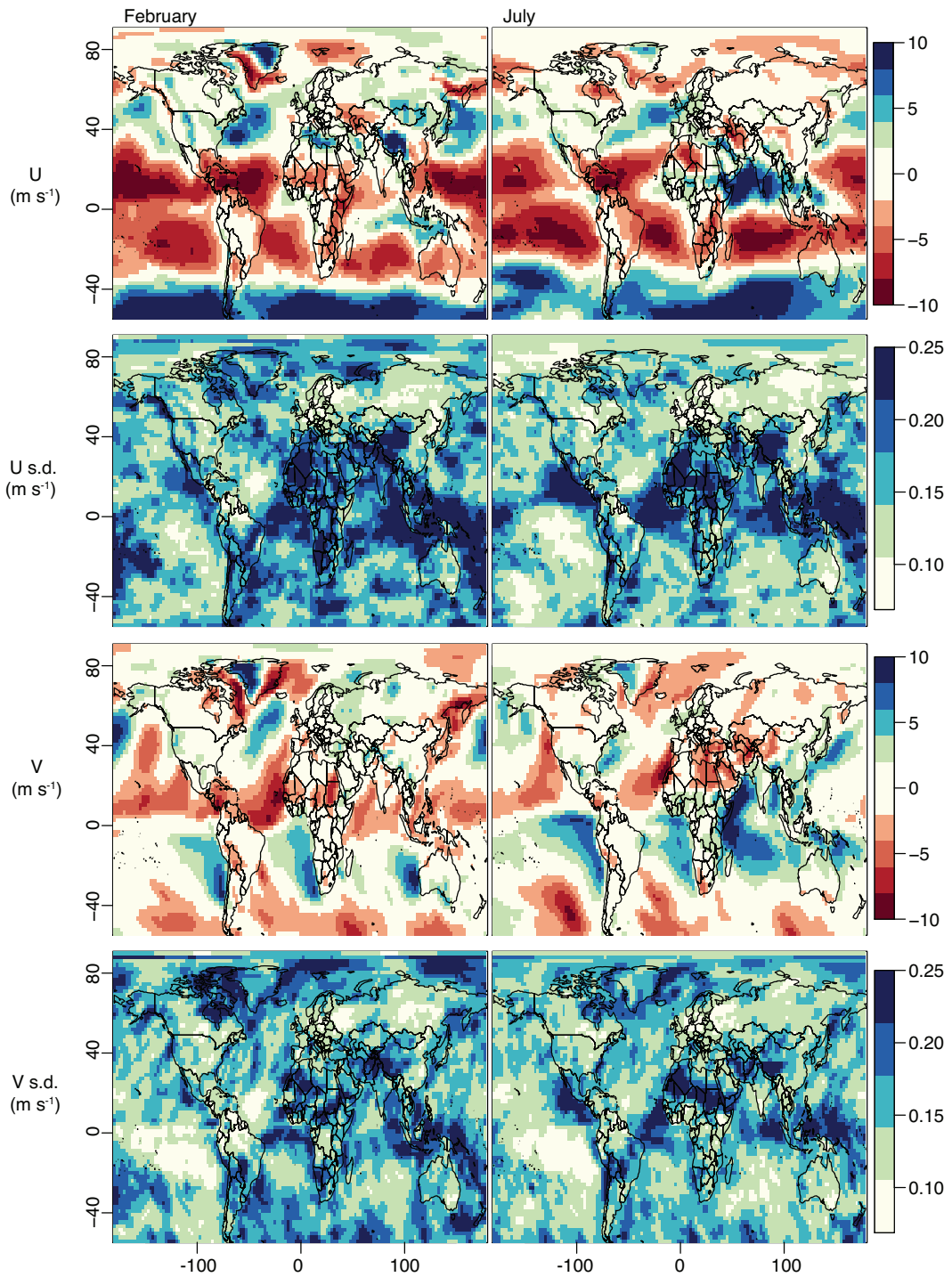


Figure S17: Maps of monthly-averaged meteorological parameters and uncertainties (standard deviations) as estimated by CAM-LETKF.

Table S2: Candidate meteorological variables

| Meteorological variable | Abbreviation | Units |
|--|----------------|-----------------------|
| Vertical velocity | Ω | Pa s^{-1} |
| Vertical velocity at 510hPa | Ω_{510} | Pa s^{-1} |
| Net longwave flux at the surface | FLNS | W m^{-2} |
| Downwelling solar flux at surface | FSDS | W m^{-2} |
| Net solar flux at surface | FSNS | W m^{-2} |
| Solar flux reflected from surface | FSRS | W m^{-2} |
| Liquid cloud water | LCWAT | kg kg^{-1} |
| Surface latent heat flux | LHFLX | W m^{-2} |
| Planetary boundary layer height | PBLH | m |
| Large-scale, stable precipitation rate | PRECL | m s^{-1} |
| Convective precipitation rate | PRECC | m s^{-1} |
| Specific humidity | Q | kg kg^{-1} |
| Relative humidity | RELHUM | % |
| Surface sensible heat flux | SHFLX | W m^{-2} |
| Net radiative flux at surface | SRFRAD | W m^{-2} |
| Temperature | T | K |
| Zonal wind | U | m s^{-1} |
| Meridional wind | V | m s^{-1} |
| Vertical diffusion diffusivity | VDD | $\text{m}^2 \text{s}$ |
| Total wind velocity | wind | m s^{-1} |

References

Anderson, J. L.: Spatially and temporally varying adaptive covariance inflation for ensemble filters, *Tellus A*, 61, 72–83, doi:10.1111/j.1600-0870.2008.00361.x, 2009.

Dee, D. P., Uppala, S. M., Simmons, A. J., Berrisford, P., Poli, P., Kobayashi, S., Andrae, U., Balmaseda, M. A., Balsamo, G., Bauer, P., Bechtold, P., Beljaars, A. C. M., van de Berg, L., Bidlot, J., Bormann, N., Delsol, C., Dragani, R., Fuentes, M., Geer, A. J., Haimberger, L., Healy, S. B., Hersbach, H., Hólm, E. V., Isaksen, L., Källberg, P., Köhler, M., Matricardi, M., McNally, A. P., Monge-Sanz, B. M., Morcrette, J.-J., Park, B.-K., Peubey, C., de Rosnay, P., Tavolato, C., Thépaut, J.-N., and Vitart, F.: The ERA-Interim reanalysis: configuration and performance of the data assimilation system, *Q. J. Roy. Meteor. Soc.*, 137, 553–597, doi:10.1002/qj.828, 2011.

Desroziers, G., Berre, L., Chapnik, B., and Poli, P.: Diagnosis of observation, background and analysis-error statistics in observation space, *Q. J. Roy. Meteor. Soc.*, 131, 3385–3396, doi:10.1256/qj.05.108, 2005.

Gerbig, C., Lin, J. C., Wofsy, S. C., Daube, B. C., Andrews, A. E., Stephens, B. B., Bakwin, P. S., and Grainger, C. A.: Toward constraining regional-scale fluxes of CO₂ with atmospheric observations over a continent: 2. Analysis of COBRA data using a receptor-oriented framework, *J. Geophys. Res. - Atmos.*, 108, 4757, doi:10.1029/2003jd003770, 2003.

Gerbig, C., Körner, S., and Lin, J. C.: Vertical mixing in atmospheric tracer transport models: error characterization and propagation, *Atmos. Chem. Phys.*, 8, 591–602, doi:10.5194/acp-8-591-2008, 2008.

Gourdji, S. M., Mueller, K. L., Yadav, V., Huntzinger, D. N., Andrews, A. E., Trudeau, M., Petron, G., Nehrkorn, T., Eluszkiewicz, J., Henderson, J., Wen, D., Lin, J., Fischer, M., Sweeney, C., and Michalak, A. M.: North American CO₂ exchange: inter-comparison of modeled estimates with results from a fine-scale atmospheric inversion, *Biogeosciences*, 9, 457–475, doi:10.5194/bg-9-457-2012, 2012.

Hunt, B. R., Kalnay, E., Kostelich, E. J., Ott, E., Patil, D. J., Sauer, T., Szunyogh, I., Yorke, J. A., and Zimin, A. V.: Four-dimensional ensemble Kalman filtering, *Tellus A*, 56, 273–277, doi:10.1111/j.1600-0870.2004.00066.x, 2004.

Hunt, B. R., Kostelich, E. J., and Szunyogh, I.: Efficient data assimilation for spatiotemporal chaos: A local ensemble transform Kalman filter, *Physica D*, 230, 112–126, doi:10.1016/j.physd.2006.11.008, 2007.

Kanamitsu, M., Ebisuzaki, W., Woollen, J., Yang, S.-K., Hnilo, J. J., Fiorino, M., and Potter, G. L.: NCEP–DOE AMIP-II Reanalysis (R-2), *B. Am. Meteorol. Soc.*, 83, 1631–1643, doi:10.1175/BAMS-83-11-1631, 2002.

Kang, J.-S., Kalnay, E., Miyoshi, T., Liu, J., and Fung, I.: Estimation of surface carbon fluxes with an advanced data assimilation methodology, *J. Geophys. Res.-Atmos.*, 117, D24101, doi:10.1029/2012JD018259, 2012.

Kretschmer, R., Gerbig, C., Karstens, U., and Koch, F.-T.: Error characterization of CO₂ vertical mixing in the atmospheric transport model WRF-VPRM, *Atmos. Chem. Phys.*, 12, 2441–2458, doi:10.5194/acp-12-2441-2012, 2012.

Li, H., Kalnay, E., and Miyoshi, T.: Simultaneous estimation of covariance inflation and observation errors within an ensemble Kalman filter, *Q. J. Roy. Meteor. Soc.*, 135, 523–533, doi:10.1002/qj.371, 2009.

Lin, J. C. and Gerbig, C.: Accounting for the effect of transport errors on tracer inversions, *Geophys. Res. Lett.*, 32, L01802, doi:10.1029/2004GL021127, 2005.

Liu, J., Fung, I., Kalnay, E., and Kang, J.-S.: CO₂ transport uncertainties from the uncertainties in meteorological fields, *Geophys. Res. Lett.*, 38, L12808, doi:10.1029/2011GL047213, 2011.

Liu, J., Fung, I., Kalnay, E., Kang, J.-S., Olsen, E. T., and Chen, L.: Simultaneous assimilation of AIRS XCO₂ and meteorological observations in a carbon climate model with an ensemble Kalman filter, *J. Geophys. Res.-Atmos.*, 117, D05309, doi:10.1029/2011JD016642, 2012.

Mesinger, F., DiMego, G., Kalnay, E., Mitchell, K., Shafran, P. C., Ebisuzaki, W., Jović, D., Woollen, J., Rogers, E., Berbery, E. H., Ek, M. B., Fan, Y., Grumbine, R., Higgins, W., Li, H., Lin, Y., Manikin, G., Parrish, D., and Shi, W.: North American Regional Reanalysis, *B. Am. Meteorol. Soc.*, 87, 343–360, doi:10.1175/BAMS-87-3-343, 2006.

MeteoSwiss Federal Office of Meteorology and Climatology: GAWSIS Station Information System, URL <http://gaw.empa.ch/gawsis/>, 2014.

Miyoshi, T.: The Gaussian approach to adaptive covariance inflation and its implementation with the Local Ensemble Transform Kalman Filter, *Mon. Weather Rev.*, 139, 1519–1535, doi:10.1175/2010MWR3570.1, 2011.

Miyoshi, T. and Kunii, M.: The Local Ensemble Transform Kalman Filter with the Weather Research and Forecasting Model: Experiments with real observations, *Pure Appl. Geophys.*, 169, 321–333, doi:10.1007/s00024-011-0373-4, 2012.

Olson, D. M., Dinerstein, E., Wikramanayake, E. D., Burgess, N. D., Powell, G. V. N., Underwood, E. C., D'amico, J. A., Itoua, I., Strand, H. E., Morrison, J. C., Loucks, C. J., Allnutt, T. F., Ricketts, T. H., Kura, Y., Lamoreux, J. F., Wettengel, W. W., Hedao, P., and Kassem, K. R.: Terrestrial Ecoregions of the World: A New Map of Life on Earth: A new global map of terrestrial ecoregions provides an innovative tool for conserving biodiversity, *BioScience*, 51, 933–938, doi:10.1641/0006-3568(2001)051[0933:TEOTWA]2.0.CO;2, 2001.

Oppenheim, A. and Schafer, R.: *Discrete-time Signal Processing*, Prentice-Hall signal processing series, Prentice Hall, 1989.

Peters, W., Jacobson, A. R., Sweeney, C., Andrews, A. E., Conway, T. J., Masarie, K., Miller, J. B., Bruhwiler, L. M. P., Petron, G., Hirsch, A. I., Worthy, D. E. J., Werf, G. R. v. d., Randerson, J. T., Wennberg, P. O., Krol, M. C., and Tans, P. P.: An atmospheric perspective on North American carbon dioxide exchange: CarbonTracker, *P. Natl. Acad. Sci. USA*, with updates documented at <http://carbontracker.noaa.gov>, 104, 18 925–18 930, doi:10.1073/pnas.0708986104, 2007.

Schuh, A. E., Denning, A. S., Corbin, K. D., Baker, I. T., Uliasz, M., Parazoo, N., Andrews, A. E., and Worthy, D. E. J.: A regional high-resolution carbon flux inversion of North America for 2004, *Biogeosciences*, 7, 1625–1644, doi:10.5194/bg-7-1625-2010, 2010.

Szunyogh, I., Kostelich, E., Gyarmati, G., Kalnay, E., Hunt, B., Ott, E., Satterfield, E., and Yorke, J.: A local ensemble transform Kalman filter data assimilation system for the NCEP global model, *Tellus A*, 60, 113–130, doi:10.1111/j.1600-0870.2007.00274.x, 2008.